nanomaterials

MDPI

Article

Measurement of the Dzyaloshinskii–Moriya Interaction in Mn_4N Films That Host Skyrmions

Wei Zhou [1], Chung Ting Ma [1,*] and S. Joseph Poon [1,2]

[1] Department of Physics, University of Virginia, Charlottesville, VA 22904, USA; wz8he@virginia.edu (W.Z.); sjp9x@virginia.edu (S.J.P.)
[2] Department of Materials Science and Engineering, University of Virginia, Charlottesville, VA 22904, USA
* Correspondence: ctm7sf@virginia.edu

Abstract: Mn_4N thin film is one of the potential magnetic mediums for spintronic devices due to its ferrimagnetism with low magnetization, large perpendicular magnetic anisotropy (PMA), thermal stability, and large domain wall velocity. Recent experiments confirmed the existence of tunable magnetic skyrmions in $MgO/Mn_4N/Cu_xPt_{1-x}$(x = 0, 0.5, 0.9, 0.95), and density functional theory (DFT) calculation provided a large theoretical value of the interfacial Dzyaloshinskii–Moriya interaction (iDMI) of Mn_4N/Pt, which is consistent with the predicted chemical trend of the DMI in transition metal/Pt films. So far, the measured DMI has not been reported in Mn_4N, which is needed in order to support the predicted large DMI value. This paper reports the average DMI of MgO/Mn_4N(17 nm)$/Cu_xPt_{1-x}$(3 nm) extracted from the anomalous Hall effect with various tilted angles, which is based on magnetic droplet theory with DMI effects. The DMI decreases from 0.267 mJ/m^2 to 0.011 mJ/m^2 with non-linear tendencies as Cu concentration in the Cu_xPt_{1-x} capping layer increases from 0 to 1, demonstrating the control of the DMI through the Cu_xPt_{1-x} capping layer. Furthermore, a solid solution model is developed based on an X-ray photoelectron spectroscopy (XPS) compositional depth profile to analyze the possible effects on the DMI from the mixing layers at the surface of Mn_4N. After taking into account the mixing layers, the large DMI in Mn_4N film with Pt capping is consistent with the predicted DMI.

Keywords: Mn_4N; DMI measurement; ferrimagnetic; mixing layer effect

Citation: Zhou, W.; Ma, C.T.; Poon, S.J. Measurement of the Dzyaloshinskii–Moriya Interaction in Mn_4N Films That Host Skyrmions. *Nanomaterials* **2023**, *13*, 1672. https://doi.org/10.3390/nano13101672

Academic Editor: Paola Tiberto

Received: 28 April 2023
Revised: 12 May 2023
Accepted: 13 May 2023
Published: 18 May 2023

1. Introduction

As information technologies keep developing, the demand for faster processing and high-density data storage is increasing [1,2]. A spintronics device, which utilizes and manipulates the spin degrees of freedom in materials, is a promising candidate for next-generation energy-efficient electronic devices with high-speed operation and ample data storage [1–5]. In a spintronic device, the magnetic medium is the critical component that determines the device's performance [2–5]. Ferrimagnetic systems with two antiparallelly coupled spin sublattices have drawn increasing attention for two reasons. The first reason is that ferrimagnetic materials have faster switching processes than ferromagnetic materials [6,7]. The other reason is the high-speed current-induced magnetic domain-wall motion in ferrimagnets [8–10].

Among numerous ferrimagnetic materials, anti-perovskite Mn_4N thin films with a Curie temperature of 710K have attracted more investigations recently [11,12]. Figure 1 shows a schematic diagram of the Mn_4N crystal structure with spins. The spins of Mn I atoms (3.47 μ_B), which sit at the corners, are ferromagnetically coupled with the spins of Mn IIa atoms (0.75 μ_B), which sit at the face center of the top and bottom surfaces in the unit cell. The spins of Mn I and Mn IIb atoms (−2.36 μ_B), which sit at the face center of side surfaces in the unit cell, are anti-ferromagnetically coupled [13]. It has been reported that the epitaxial Mn_4N thin films grown on various substrates, such as MgO(001), STO(001), $LaAlO_3$(001), and LSTO(001) [10,13–19], exhibit perpendicular magnetic anisotropy (PMA), which is

essential for some spintronic devices. The magnetization of Mn_4N thin films is tunable by doping Ni ($Mn_{4-x}Ni_xN$) or Co ($Mn_{4-x}Co_xN$), and magnetic compensation (zero net magnetization) can be achieved with suitable Ni or Co composition [20–22]. More importantly, compared to ferrimagnetic rare-earth transition metal amorphous thin films, the Mn_4N thin films have better thermal stability because Mn_4N films are deposited at 400–450 °C, and no structural transition or loss of PMA has been reported after annealing and cooling processes. Furthermore, experiments have reported high domain wall velocity(~1 km/s) [10,23], high spin polarization (0.8) [22], and magnetic skyrmions in Mn_4N [23], which indicates that the Mn_4N thin film is a potential material for spintronic devices, such as racetrack memory and skyrmion-based magnetic tunnel junctions [24,25]. Additionally, the skyrmions' diameter in $MgO(001)/Mn_4N/Cu_xPt_{1-x}$ can be tuned by changing the composition of the capping layer, which would vary the interfacial Dzyaloshinskii–Moriya interaction (iDMI) [23].

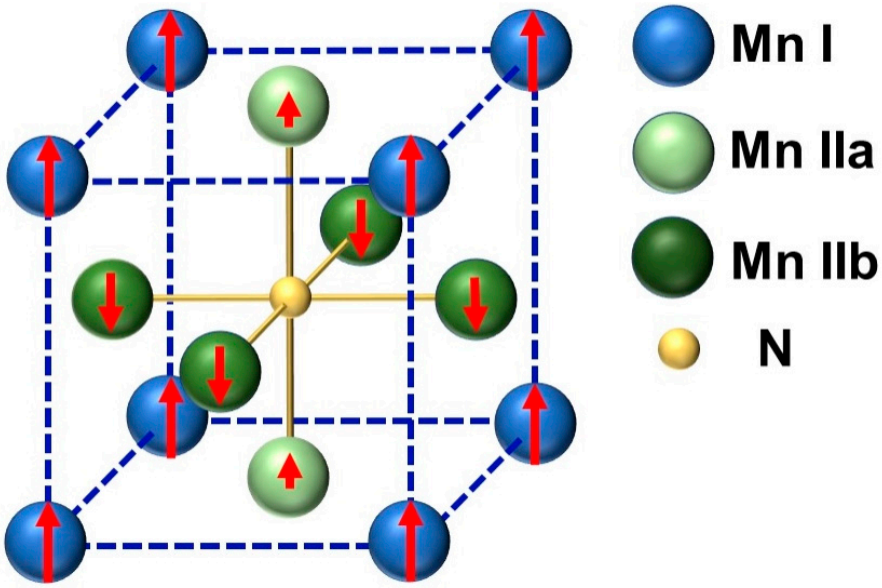

Figure 1. A schematic diagram of the Mn_4N crystal structure.

The iDMI is an antisymmetric exchange interaction that favors the noncolinear alignments of neighboring spins [26,27]. It arises from the spin–orbit coupling at magnetic layer interfaces with broken inversion symmetry. The iDMI, which has attracted great interest in recent years, is one of the crucial interactions to develop new promising spintronic applications [27]. For example, the iDMI is vital in stabilizing topologically non-trivial chiral magnetic textures, such as Néel magnetic skyrmions and chiral domain walls [3,4,26], which are candidates to serve as building blocks in data storage. In addition, the interplay of DMI and spin–orbit torque (SOT) provides a fast and power-saving method of field-free current-induced switching of perpendicular magnetization, which is critical in low-energy and high-speed calculations [28,29].

It has been predicted by first-principle calculations that, at the interface of 3D transition metals (TMs) (V, Cr, Mn, Fe, Co, Ni) and 5D heavy metals (HMs) (W, Re, Os, Ir, Pt), the 3D orbit occupation of TMs serves an important role in the strength of the DMI. The Mn element has the largest DMI due to its half-filled 3D band [30]. While many DMI measurements have been applied to often studied Co and Co-based films with HM interface [31–39], no measured DMI of Mn or Mn-based magnetic films has been reported to support the systematic trend of increasing the iDMI. Additionally, density functional theory (DFT) has predicted a large iDMI at the Mn_4N/Pt interface, where DMI is only considered between the Mn nearest neighbors (Mn I and Mn IIa atoms) at the Mn_4N/Pt interface [23]. Thus, the experimental DMI in Mn_4N is necessary to confirm the calculations and comprehensively explore the material for applications. Kim et al. developed a method, based on magnetic droplet theory with the DMI effect, to extract the average DMI from

in-plane field dependence of the out-of-plane nucleation field for a reversed domain. This method can be completed with a magnetoresistance measurement setup or a magneto-optical Kerr effect (MOKE) microscope [40]. Here, to confirm the calculated large Mn_4N DMI and comprehensively explore the material for spintronic applications, the DMI of $MgO/Mn_4N(17\ nm)/Cu_xPt_{1-x}$ (x = 0, 0.5, 0.9, 1) is determined by extracting the effective field of the DMI from the angular dependence anomalous Hall effect. The average DMI of the $MgO/Mn_4N/Cu_xPt_{1-x}$ decreases non-linearly from 0.267 mJ/m^2 to 0.011 mJ/m^2 as Cu concentration increases from 0 to 1. Furthermore, $MgO/Mn_4N(17\ nm)/Pt$ has a larger interfacial DMI constant (Ds) than MgO/Co(0.5–1.2 nm)/Pt film [31–39], where Ds is the product of the average DMI and the thickness of the magnetic layer. The larger Ds of $MgO/Mn_4N/Pt$ is consistent with the DMI trend calculated by A. Belabbes et al. [30]. Moreover, the possible effect on the DMI of the mixing layer at the surface of Mn_4N is discussed. The multilayers are divided into tens of sublayers using a compositional gradient. The composition of each sublayer is estimated by X-ray photoelectron spectroscopy (XPS). A solid solution model is used to calculate the average DMI of $MgO/Mn_4N(17\ nm)/Cu_xPt_{1-x}$, which incorporates the effect from the mixing layers at the surfaces of Mn_4N layers.

2. Materials and Methods

Seventeen-nm-thick Mn_4N thin films were deposited on the MgO(001) 5 × 5 × 0.5 mm substrate by reactive radio frequency (rf) sputtering at 450 °C. The MgO substrates were wet-cleaned and heat-treated ex situ. The base pressure was 5×10^{-8} Torr and the deposition pressure was 1×10^{-3} Torr. The flow rates ratio of Ar and N_2 gases was maintained at a flow rate ratio of 93:7. Three-nm-thick capping layers of Cu_xPt_{1-x} (where x = 1, 0.5, 0.1, 0) were deposited on the Mn_4N layer at room temperature by co-sputtering Pt and Cu targets to tune the DMI. Then, a 3 nm-thick Pt layer is deposited on top to prevent oxidation. The structure of the films is shown in Figure 2a. Details of the deposition process and cleaning MgO substrates were reported in a previous work [18]. The composition of the capping layers was calibrated with 10 nm-thick Cu_xPt_{1-x} films on MgO(100) substrates using PHI VersaProbe III X-ray photoelectron spectroscopy (XPS). The out-of-plane and in-plane magnetic hysteresis loops of each sample were measured at 300 K by a Quantum Design VersaLab III vibrating sample magnetometer (VSM). The Mn_4N films were patterned into a 5 μm-wide Hall cross-structure by photolithography and an Ar ion milling technique. A 100 nm-thick Pt layer was deposited on the patterned samples as contact pads for anomalous Hall effect (AHE) measurements.

We measured the average DMI using the method proposed by Kim et al., which is based on the magnetic droplet nucleation model [40]. The schematic of the measurement setup is shown in Figure 2b. The angular-dependent coercivity field H_c of the Mn_4N Hall cross-structure was measured. By definition, the perpendicular component (H_z) and in-plane component (H_x) of H_c are given by $H_z \equiv H_c \cos\theta$ and $H_x \equiv H_c \sin\theta$, where θ is the angle between the external magnetic field (H) and the normal sample. θ varied from 0° to 65° in this experiment. The external magnetic field was swept within ± 2 T at each angle to observe the coercivity field H_c. Figure 2d shows normalized anomalous Hall effect loops of $MgO/Mn_4N/Pt$ with different tilted angles θ. With the DMI, there is a threshold point in the $H_z^{1/2}$ vs. the H_x curve, where $H_z^{1/2}$ begins to decrease linearly with increasing H_x. This threshold point corresponds to the effective magnetic field induced by DMI(H_{DMI}).

XPS measurements were performed to obtain the compositional depth profile using the PHI VersaProbe III XPS instrument. XPS data were collected after sputtering off a few layers from the surface. Each sputtering lasted 15 s, and the total sputtering time was 10 min. The analysis method followed the method in [41].

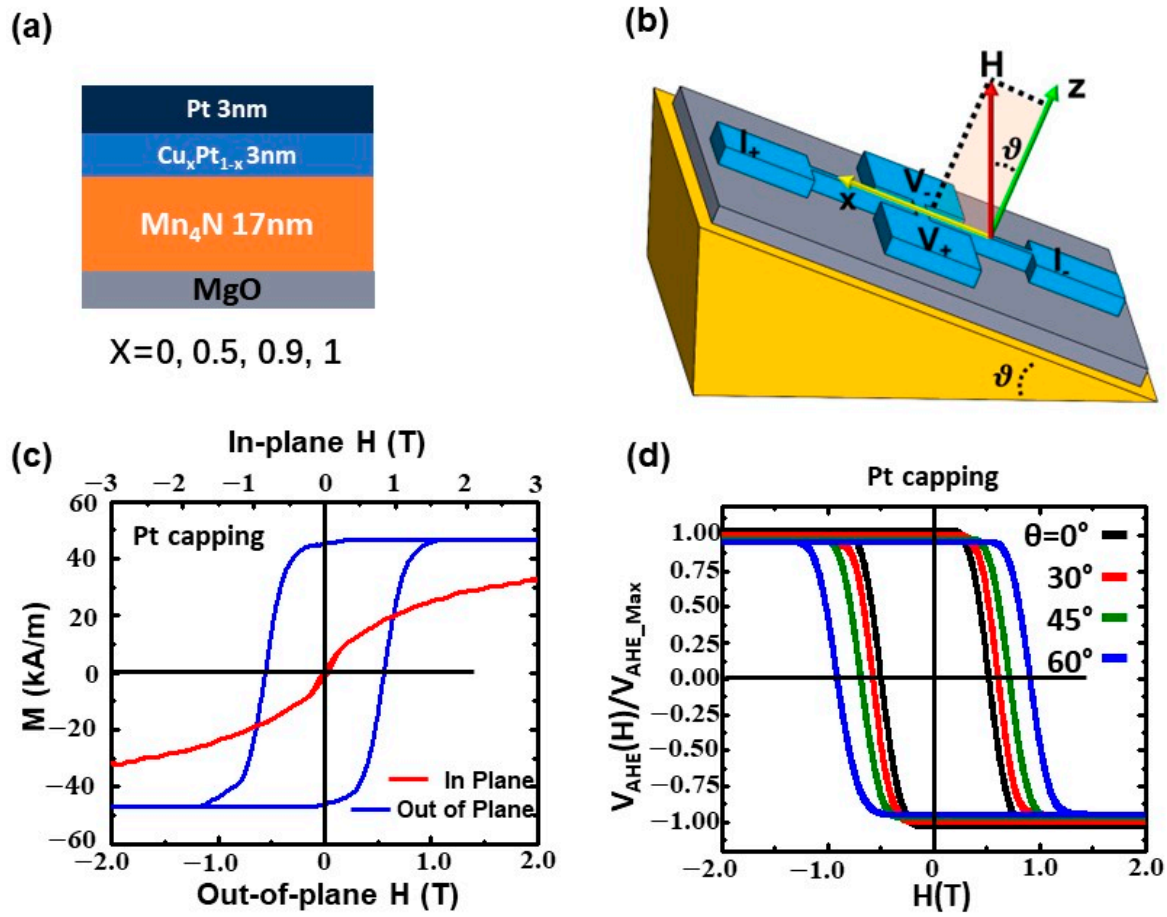

Figure 2. (**a**) Structure of the samples MgO(100)/Mn_4N(17 nm)/Cu_xPt_{1-x}(3 nm)/ Pt(3 nm). (**b**) Schematic setup of the DMI measurement. The samples were put on a titled holder while the external magnetic field (H) was applied in the vertical direction. The out-of-plane component H_z and the in-plane component H_x of the coercivity field H_c were calculated with $H_z \equiv H_c \cos\theta$ and $H_x \equiv H_c \sin\theta$. The range of the tilted angle θ was 0–65°. (**c**) M(H) loops of MgO/Mn_4N/Pt with an out-of-plane external magnetic field and an in-plane external magnetic field were measured by VSM. (**d**) Normalized anomalous Hall voltage (V_{AHE}) loops of MgO/Mn_4N/Pt with different tilted angles (θ = 0° (black), 30° (red), 45° (green), 60° (blue)).

3. Results and Discussion

3.1. DMI Measurement

Figure 3a–d show the $H_z^{1/2}$ vs. H_x curves of capping layers with different Cu compositions (x) (x = 0, 0.5, 0.9, 1). The lines in the graphs are the fitted lines. The turning points correspond to the H_{DMI} of each capping layer. As the Cu concentration of the capping layer(x) increases, the $H_z^{1/2}$ begins to decrease linearly at a lower $H_z^{1/2}$. This means that H_{DMI} decreases and the average DMI decreases. This trend matches the previously reported tunable size of skyrmions in Mn_4N with Cu_xPt_{1-x} capping, where the size of the magnetic skyrmion in MgO/Mn_4N/Cu_xPt_{1-x} decreases as the Cu concentration increases [24]. This agrees with the intuition that smaller *DMI* produces smaller skyrmions [24]. The DMIs of different capping layers are calculated based on the following equation:

$$\mathrm{DMI} = \sqrt{A/K_{eff}}M_s H_{DMI} \quad (1)$$

where A is the exchange stiffness, K_{eff} is the effective perpendicular magnetic anisotropy energy, and M_s is the saturation magnetization. For Mn_4N, A is 18 pJ/m [10] and M_s and K_{eff} are 47 kA/m and 1.05 × 10^5 J/m^3, respectively, based on the VSM measurement of

$MgO/Mn_4N/Pt$. The measured DMIs of different capping layers are plotted in Figure 3e. The errors in the measured DMI mostly come from the uncertainties of the tilted angle and fitting. As Cu concentration rises, the DMI decreases from 0.267 ± 0.065 mJ/m^2 to 0.011 ± 0.01 mJ/m^2. This decrease in DMI can be explained by two reasons. First, the addition of Cu diluted the concentration of Pt, which reduced the large iDMI at the interface of Pt/Mn_4N. Second, the iDMI at the Cu/Mn_4N interface is small and has the opposite sign of the iDMI at the Pt/Mn_4N interface. This would further decrease the iDMI as Cu concentration increases. We note that the decrease in the DMI is not linear as a function of Cu composition x. When x increases from 0 to 0.5, the DMI decreases from 0.267 ± 0.065 mJ/m^2 to 0.224 ± 0.053 mJ/m^2. Compared to the large change in the CuPt capping layer composition, the change in the DMI is small and the difference is within the measurement error. This indicates that when the Cu concentration is smaller than 0.5, the DMI is almost insensitive to the change in Cu concentration. When x further increases to 0.9, the DMI decreases to 0.115 ± 0.041 mJ/m^2, which is about half of the DMI when x is 0.5. When it is pure Cu capping (x = 1), the DMI decreases more to near zero. Since a small amount of Pt in the capping layer can provide a large DMI, it indicates that the DMI is more sensitive to the Pt concentration than the Cu concentration. This can be explained by the larger spin–orbit coupling (SOC) between Pt and Mn than the SOC between Cu and Mn [23,42]. The non-linear composition dependence of the DMI has also been reported in $Pt/CoGd/W_xPt_{1-x}$ [43]. Since DMIs in these thin films are interfacial effects originating from the interface, the measured DMIs decrease with thicker magnetic layers. To compare the DMI with other materials that have different thicknesses, we use the interfacial DMI constant Ds, where Ds is the average DMI multiplied by the magnetic layer thickness(t_m). The result is shown in Figure 3f; the Mn_4N data point is from our measurement of $MgO/Mn_4N/Pt$ and the Co data point is the average of several reported Ds in the Co single layer with different thicknesses sandwiched by MgO and Pt, where the error bar is the standard deviation [31–39]. The Ds of $MgO/Mn_4N/Pt$ is about twice the Ds of MgO/Co/Pt, which is consistent with the chemical trend of the DMI in transition metals from first-principle calculations [30].

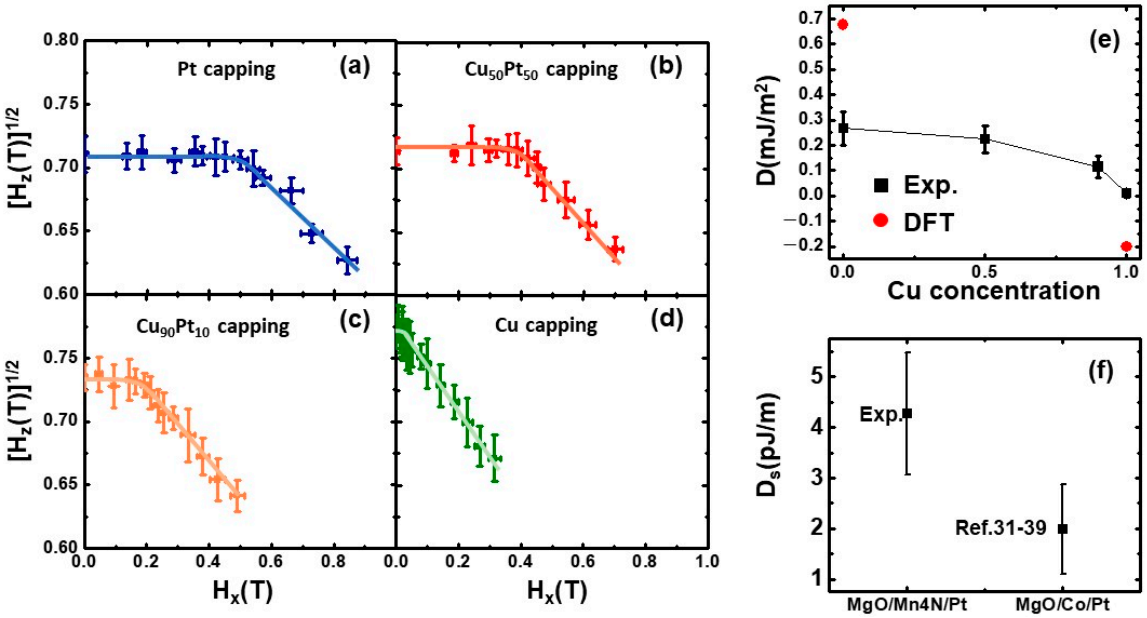

Figure 3. (**a**–**d**) $H_z^{1/2}$ vs. H_x curves of $MgO/Mn_4N/CuxPt_{1-x}$ with different capping layers x = 0, 0.5, 0.9, 1. The lines in the graphs are the fitted lines. The turning points, where $H_z^{1/2}$ begins to decrease linearly vs. H_x, correspond to the H_{DMI} of each capping. (**e**) The measured DMI of $MgO/Mn_4N/Cu_xPt_{1-x}$ with different Cu concentrations in the capping layers. Red dots indicate the DMI from DFT calculations. (**f**) D_s comparison between $MgO/Mn_4N/Pt$ and MgO/Co/Pt [31–39].

The measured DMI of MgO/Mn4N/Pt (0.267 mJ/m^2) is one magnitude smaller than the DFT-predicted iDMI of Mn_4N/Pt (6.969 m J/m^2) [23]. The reason is that the calculated iDMI is based on Mn_4N [23] or Mn [33] ultrathin films, while our measurement was performed on a 17 nm-thick film. The DMI we measured is the average DMI over the film. As mentioned previously, since the predicted iDMI is an interfacial effect and decays away from the surface, the average DMI decreases significantly as the thickness increases and is much smaller than the predicted iDMI. To further investigate the relationship between our measured DMI and predicted DMI, we conducted a detailed comparison of the DMIs. In Figure 3e, the red dots correspond to the average DMI ($D_{average}$) in MgO/Mn_4N/Pt and MgO/Mn_4N/Cu obtained from DFT calculations [23].

$$D_{average} = \int_0^{t_m} D(t)dt/t_m \tag{2}$$

$$D(t) = D_0 \begin{cases} e^{\frac{0.4-t}{0.4}}, & t > 0.4 \\ 1, & t < 0.4 \end{cases} \tag{3}$$

where *D(t)* is the DMI distribution function, which describes the exponentially decaying iDMI from the surface [44]. D_0 is the iDMI at the surface from the DFT [23], as shown in Table 1, and t is the distance from the surface in nm. As seen in Figure 3e, there is a clear discrepancy between the calculated DMI and the experimental DMI. One of the possible reasons is the presence of the mixing layers at the Mn_4N interfaces. In the DFT, the interface between two layers is assumed to be an ideal surface, which means that there are no atomic mixings. However, XPS and polarized neutron reflectometry (PNR) found that the interfaces of Mn_4N/Pt and MgO/Mn_4N are not ideal [41]. There are 3–4 nm of mixing layers present at the interfaces, including some MnO at the surface of Mn_4N. These mixing layers at the interface decrease the accuracy of the iDMI from the DFT calculation, which can explain the discrepancy between the predicted DMI and the measured DMI.

Table 1. The interfacial DMI at the surface of MgO/Mn_4N, Pt/Mn_4N (001), and Cu/Mn_4N (001), calculated by the DFT [23].

MgO/Mn_4N (001)	**Pt/Mn_4N (001)**	**Cu/Mn_4N (001)**
−1.017 mJ/m^2	6.969 mJ/m^2	−2.633 mJ/m^2

3.2. Mixing Layer Effect on the DMI

To investigate the possible effect of the mixing layers on the DMI, a solid solution model is built. In this model, the multilayer is divided into tens of sublayers with a thickness of 0.4 nm, as shown in Figure 4. The composition of each sublayer is estimated by XPS data using the method by Ma et al. [43]. There are two assumptions in this model. First, the DMI between the two sublayers is originated from the interactions between Cu, Pt, and Mg in one layer ($L_{n'}$) and Mn atoms the other layer (L_n). This means that the DMI is proportional to the concentration of Pt($y_{n'}$) in layer $L_{n'}$ and the concentration of Mn(z_n) of L_n. It is the same for the DMI between Cu and Mn, or Mg and Mn. Second, the DMI from one sublayer L_n decays exponentially from the surface of layer L_n, which is given by Equation (2).

The total DMI from Pt acting on a sublayer L_n (DMI_{Pt-L_n}) is the sum of the DMI of Pt from all over other sublayers:

$$DMI_{Pt-L_n} = \sum_{n',n' \neq n} z_n * y_{n'} * D_{n,n'} S_{n,n'} \tag{4}$$

$$D_{n,n'} = D_{0-Pt/Mn4N} \begin{cases} e^{\frac{0.4-|t_n - t_{n'}|}{0.4}}, |t_n - t_{n'}| > 0.4 \\ 1, |t_n - t_{n'}| < 0.4 \end{cases} \tag{5}$$

$$S_{n,n'} = \begin{cases} 1, t_n < t_{n'} \\ -1, t_{n'} < t_n \end{cases} \quad (6)$$

where $D_{0-Pt/Mn4N}$ is the calculated DMI at the Pt/Mn_4N interface [24], as shown in Table 1, and $S_{n,n'}$ is a function that assigns the direction of the DMI. The DMI from the *Pt* atoms under the layer L_n ($t_{n'} < t_n$) has an opposite sign compared to the DMI from the *Pt* atoms above the layer L_n ($t_n < t_{n'}$).

The total average DMI from *Pt* (DMI_{Pt}) is the sum from all layers, *n*:

$$DMI_{Pt} = \sum_n DMI_{Pt-L_n} * 0.4/T \quad (7)$$

where *T* is the total thickness of the samples. The same method was used to calculate the total average DMI from Cu (DMI_{Cu}) and Mg (DMI_{Mg}). The total DMI (DMI_{tot}) in the film is given in Equation (7) as the sum of the DMI from Pt, Cu, and Mg.

$$DMI_{tot} = DMI_{Pt} + DMI_{Cu} + DMI_{Mg} \quad (8)$$

Figure 5a–d show the compositional depth profiles of Mn_4N with various Cu_xPt_{1-x} capping layers obtained from the analysis of XPS measurements. Figure 5a is obtained from our previous publication on the mixing layers in MgO/Mn_4N/Pt [41]. Here, the surface of the Pt layer is set at z = 0 nm. The depth profile shows that elemental mixings exist at all the interfaces (Pt/Cu_xPt_{1-x}, Cu_xPt_{1-x}/Mn_4N, and Mn_4N/MgO). The diffusion from the protective Pt layer on top of the Cu_xPt_{1-x} capping layer increases the actual Pt concentration in Cu_xPt_{1-x}, and consequently increases the Pt diffusion into Mn_4N. Based on the compositional depth profile in Figure 5b–d, using z = 4 nm as a reference point, the actual Cu:Pt ratio of the capping layer is 41:54 for the $Cu_{50}Pt_{50}$ capping sample. It is 64:22 for the $Cu_{90}Pt_{10}$ capping sample and 77:13 for the Cu capping sample. From all four profiles, oxygen peaks are found to exist near the top surface of Mn_4N (z < 7 nm), and the Mg:O ratio near the bottom surface (z > 20 nm) is smaller than 50:50. These indicate that both the Cu_xPt_{1-x}/Mn_4N and Mn_4N/MgO interface have some MnO. The presence of MnO at the Cu_xPt_{1-x}/Mn_4N originated from oxidization during the cooling process between the Mn_4N deposition and CuPt deposition, and the MnO at the surface of Mn_4N/MgO is due to the oxygen diffusion from the MgO substrate to the Mn_4N layer [41]. Using the compositional depth profile in Figure 5a–d, the average DMIs of MgO/Mn_4N/Cu_xPt_{1-x} were estimated by the solid solution model. Figure 5e shows the comparison between the calculated DMI using the solid solution model and the measured DMI. The calculated DMIs, which are indicated by the green triangles, are in agreement with the measured DMIs, indicated by black squares.

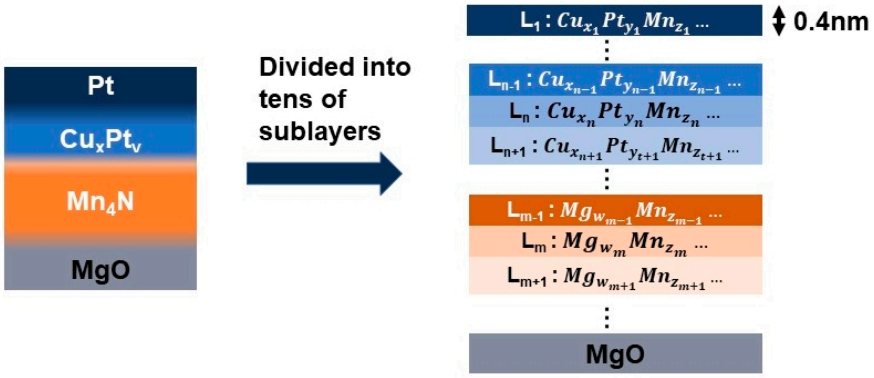

Figure 4. A schematic diagram of the solid solution model. A sample is divided into tens of sublayers with a thickness of 0.4 nm using a compositional gradient.

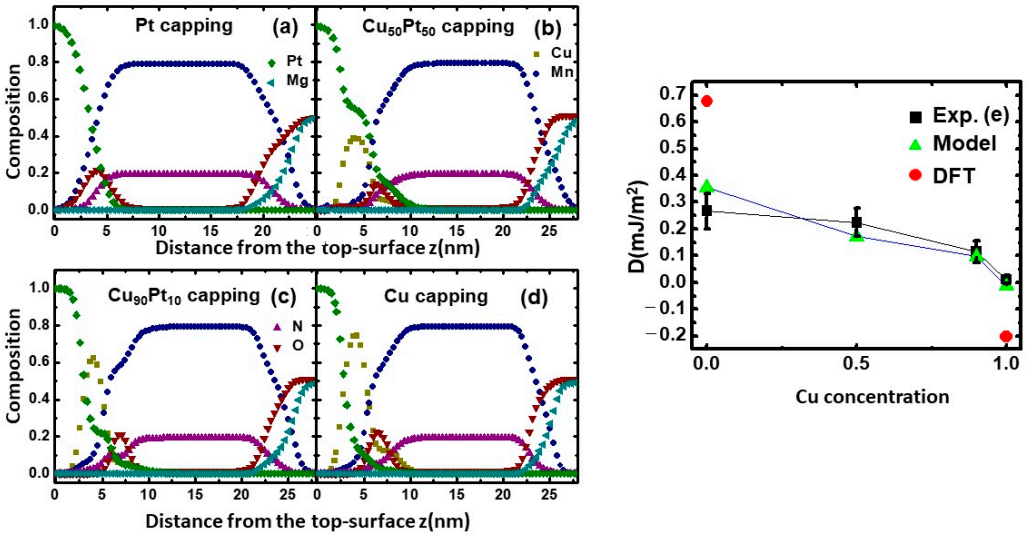

Figure 5. (**a**–**d**) A compositional depth profile of Mn_4N samples with different capping layers as a function of distance from the Pt protective layer obtained from an analysis of XPS measurements. (**a**) Is obtained from [41]. (**e**) A comparison of the calculated DMI from the solid solution model (green), measured DMI (black), and average DMI based on the DFT (red).

4. Conclusions

The Dzyaloshinskii–Moriya interactions (DMIs) of $MgO/Mn_4N/Cu_xPt_{1-x}$ multilayers were measured by extracting H_{DMI} from the angular dependence of the coercivity field based on the magnetic droplet nucleation model. The compositional dependence of the DMI is non-linear in Cu concentrations. The interfacial DMI constant D_s of $MgO/Mn_4N/Pt$ is larger than that of MgO/Co/Pt, which is consistent with the chemical trend of the DMI among the transition metals. To study the effect of mixing layers on the DMI, a simple solid solution model with the mixing layers effect is built, based on the X-ray photoelectron spectroscopy (XPS) measurement, and the average DMI from this model is in good agreement with the measured DMI. Our experimental results provide a promising approach to control the DMI in Mn_4N-based thin films, with implications in achieving small skyrmion and enabling future spintronics technologies. Our results also provide a method to connect the density functional theory (DFT), calculated DMI, and measured DMI.

Author Contributions: W.Z.: sample fabrication, measurements, modeling, and writing—original draft. C.T.M.: modeling and writing—review and editing. S.J.P.: funding acquisition (lead), supervision (lead), and writing—review and editing. All authors have read and agreed to the published version of the manuscript.

Funding: This work was supported by the DARPA Topological Excitations in Electronics (TEE) program (grant D18AP00009). The content of the information does not necessarily reflect the position or the policy of the government, and no official endorsement should be inferred. Approved for public release; distribution is unlimited.

Institutional Review Board Statement: Not applicable.

Informed Consent Statement: Not applicable.

Data Availability Statement: The data that support the findings of this study are available from the corresponding author upon reasonable request.

Acknowledgments: The Phi VersaProbe III XPS used for acquiring the data was provided by the NSF-MRI Award No. 1626201.

Conflicts of Interest: The authors declare no conflict of interest.

References

1. Dieny, B.; Prejbeanu, I.L.; Garello, K.; Gambardella, P.; Freitas, P.; Lehndorff, R.; Raberg, W.; Ebels, U.; Demokritov, S.O.; Akerman, J.; et al. Opportunities and challenges for spintronics in the microelectronics industry. *Nat. Electron.* **2020**, *3*, 446–459. [CrossRef]
2. Jungwirth, T.; Marti, X.; Wadley, P.; Wunderlich, J. Antiferromagnetic spintronics. *Nat. Nanotechnol.* **2016**, *11*, 231–241. [CrossRef] [PubMed]
3. Zhang, Y.; Feng, X.; Vallobra, P.; He, Y.; Wang, Z.; Chen, L.; Zhang, K.; Zhao, W. Ferrimagnets for spintronic devices: From materials to applications. *Appl. Phys. Lett.* **2023**, *10*, 011301. [CrossRef]
4. Žutić, I.; Fabian, J.; Sarma, S.D. Spintronics: Fundamentals and applications. *Rev. Mod. Phys.* **2004**, *76*, 323. [CrossRef]
5. Barla, P.; Joshi, V.K.; Bhat, S. Spintronic devices: A promising alternative to CMOS devices. *J. Comput. Electron.* **2021**, *20*, 805–837. [CrossRef]
6. Amal, E.G.; Jon, G.; Richard, B.W.; Akshay, P.; Jeffrey, B. Progress towards ultrafast spintronics applications. *J. Magn. Magn. Mater.* **2020**, *502*, 166478. [CrossRef]
7. Stanciu, C.D.; Tsukamoto, A.; Kimel, A.V.; Hansteen, F.; Kirilyuk, A.; Itoh, A.; Rasing, T. Subpicosecond Magnetization Reversal across Ferrimagnetic Compensation Point. *Phys. Rev. Lett.* **2007**, *99*, 217204. [CrossRef]
8. Siddiqui, S.A.; Han, J.; Finley, J.T.; Hansteen, F.; Kirilyuk, A.; Itoh, A.; Rasing, T. Current-Induced Domain Wall Motion in a Compensated Ferrimagnet. *Phys. Rev. Lett.* **2018**, *121*, 057701. [CrossRef]
9. Caretta, L.; Mann, M.; Büttner, F.; Ueda, K.; Pfau, B.; Günther, C.M.; Hessing, P.; Churikova, A.; Klose, C.; Schneider, M.; et al. Fast current-driven domain walls and small skyrmions in a compensated ferrimagnet. *Nat. Nanotechnol.* **2018**, *13*, 1154–1160. [CrossRef]
10. Gushi, T.; Klug, M.J.; Garcia, J.P.; Ghosh, S.; Attané, J.P.; Okuno, H.; Fruchart, O.; Vogel, J.; Suemasu, T.; Pizzini, S.; et al. Large Current Driven Domain Wall Mobility and Gate Tuning of Coercivity in Ferrimagnetic Mn_4N Thin Films. *Nano Lett.* **2019**, *19*, 8716–8723. [CrossRef]
11. Zhang, Z.; Mi, W. Progress in ferrimagnetic Mn_4N films and its heterostructures for spintronics applications. *J. Phys. D Appl. Phys.* **2022**, *55*, 013001. [CrossRef]
12. Suemasu, T.; Vila, L.; Attané, J.P. Present Status of Rare-earth Free Ferrimagnet Mn_4N and Future Prospects of Mn_4N-based Compensated Ferrimagnets. *J. Phys. Soc. Jpn.* **2021**, *90*, 081010. [CrossRef]
13. Zhou, W.; Ma, C.T.; Hartnett, T.Q.; Balachandran, P.V.; Poon, S.J. Rare-earth-free ferrimagnetic mn4n sub-20 nm thin films as potential high-temperature spintronic material. *AIP Adv.* **2021**, *11*, 015334. [CrossRef]
14. Shen, X.; Chikamatsu, A.; Shigematsu, K.; Hirose, Y.; Fukumura, T.; Hasegawa, T. Metallic transport and large anomalous hall effect at room temperature in ferrimagnetic Mn_4N epitaxial thin film. *Appl. Phys. Lett.* **2014**, *105*, 072410. [CrossRef]
15. Yasutomi, Y.; Ito, K.; Sanai, T.; Toko, K.; Suemasu, T. Perpendicular magnetic anisotropy of Mn_4N films on MgO(001) and SrTiO3(001) substrates. *J. Appl. Phys.* **2014**, *115*, 17A935. [CrossRef]
16. Kabara, K.; Tsunoda, M. Perpendicular magnetic anisotropy of Mn_4N films fabricated by reactive sputtering method. *J. Appl. Phys.* **2015**, *117*, 17B512. [CrossRef]
17. Foley, A.; Corbett, J.; Khan, A.; Richard, A.L.; Ingram, D.C.; Smith, A.R.; Zhao, L.; Gallagher, J.C.; Yang, F. Contribution from ising domains overlapping out-of-plane to perpendicular magnetic anisotropy in Mn_4N thin films on MgO(001). *J. Magn. Magn. Mater.* **2017**, *439*, 236. [CrossRef]
18. Hirose, T.; Komori, T.; Gushi, T.; Anzai, A.; Toko, K.; Suemasu, T. Strong correlation between uniaxial magnetic anisotropic constant and in-plane tensile strain in Mn_4N epitaxial films. *AIP Adv.* **2020**, *10*, 025117. [CrossRef]
19. Isogami, S.; Masuda, K.; Miura, Y. Contributions of magnetic structure and nitrogen to perpendicular magnetocrystalline anisotropy in antiperovskite $\varepsilon-Mn_4N$. *Phys. Rev. Mater.* **2020**, *4*, 014406. [CrossRef]
20. Komori, T.; Gushi, T.; Anzai, A.; Vila, L.; Attané, J.P.; Pizzini, S.; Vogel, J.; Isogami, S.; Toko, K.; Suemasu, T. Magnetic and magneto-transport properties of Mn_4N thin films by Ni substitution and their possibility of magnetic compensation. *J. Appl. Phys.* **2019**, *125*, 213902. [CrossRef]
21. Mitarai, H.; Komori, T.; Hirose, T.; Ito, K.; Ghosh, S.; Honda, S.; Toko, K.; Vila, L.; Attané, J.P.; Amemiya, K.; et al. Magnetic compensation at two different composition ratios in rare-earth-free $Mn_{4-x}Co_xN$ ferrimagnetic films. *Phys. Rev. Mater.* **2020**, *4*, 094401. [CrossRef]
22. Ghosh, S.; Komori, T.; Hallal, A.; Garcia, J.P.; Gushi Hirose, T.; Mitarai, H.; Okuno, H.; Vogel, J.; Chshiev, M.; Attané, J.P.; et al. Current-Driven Domain Wall Dynamics in Ferrimagnetic Nickel-Doped Mn_4N Films: Very Large Domain Wall Velocities and Reversal of Motion Direction across the Magnetic Compensation Point. *Nano Lett.* **2021**, *6*, 2580–2587. [CrossRef]
23. Ma, C.T.; Zhou, W.; Hartnett, T.Q.; Balachandran, P.V.; Poon, S.J. Tunable magnetic skyrmions in ferrimagnetic Mn_4N. *Appl. Phys. Lett.* **2021**, *119*, 192406. [CrossRef]
24. Fert, A.; Reyren, N.; Cros, V. Magnetic skyrmions: Advances in physics and potential applications. *Nat. Rev. Mater.* **2017**, *2*, 17031. [CrossRef]
25. Everschor-Sitte, K.; Masell, J.; Reeve, R.M.; Kläui, M. Perspective: Magnetic skyrmions—Overview of recent progress in an active research field. *J. Appl. Phys.* **2018**, *124*, 240901. [CrossRef]
26. Jiang, W.J.; Chen, G.; Liu, K.; Zang, J.; Velthuis, S.G.E.; Hoffmann, A. Skyrmions in magnetic multilayers. *Phys. Rep.* **2017**, *704*, 1–49. [CrossRef]

27. Kuepferling, M.; Casiraghi, A.; Soares, G.; Durin, G. Measuring interfacial Dzyaloshinskii-Moriya interaction in ultrathin magnetic films. *Rev. Mod. Phys.* **2023**, *95*, 015003. [CrossRef]
28. He, W.; Wan, C.; Zheng, C.; Wang, Y.; Wang, X.; Ma, T.; Wang, Y.; Guo, C.; Luo, X.; Stebliy, M.E.; et al. Field-Free Spin–Orbit Torque Switching Enabled by the Interlayer Dzyaloshinskii–Moriya Interaction. *Nano Lett.* **2022**, *22*, 6857–6865. [CrossRef]
29. Zheng, Z.; Zhang, Y.; Lopez-Dominguez, V.; Sánchez-Tejerina, L.; Shi, J.; Feng, X.; Chen, L.; Wang, Z.; Zhang, Z.; Zhang, K.; et al. Field-free spin-orbit torque-induced switching of perpendicular magnetization in a ferrimagnetic layer with a vertical composition gradient. *Nat. Commun.* **2021**, *12*, 4555. [CrossRef]
30. Belabbes, A.; Bihlmayer, G.; Bechstedt, F.; Blügel, S.; Manchon, A. Hund's Rule-Driven Dzyaloshinskii-Moriya Interaction at 3d−5dInterfaces. *Phys. Rev. Lett.* **2016**, *117*, 247202. [CrossRef]
31. Boulle, O.; Vogel, J.; Yang, H.; Pizzini, S.; Chaves, D.S.; Locatelli, A.; Menteş, T.O.; Sala, A.; Buda-Prejbeanu, L.D.; Klein, O.; et al. Room-temperature chiral magnetic skyrmions in ultrathin magnetic nanostructures. *Nat. Nanotech.* **2016**, *11*, 449–454. [CrossRef] [PubMed]
32. Cao, A.; Zhang, X.; Koopmans, B.; Peng, S.; Zhang, Y.; Wang, Z.; Yan, S.; Yang, H.; Zhao, W. Tuning the Dzyaloshinskii–Moriya interaction in Pt/Co/MgO heterostructures through the MgO thickness. *Nanoscale* **2018**, *10*, 12062–12067. [CrossRef] [PubMed]
33. Kim, S.; Ueda, K.; Go, G.; Jang, P.H.; Lee, K.J.; Belabbes, A.; Manchon, A.; Suzuki, M.; Kotani, Y.; Nakamura, T.; et al. Correlation of the Dzyaloshinskii–Moriya interaction with Heisenberg exchange and orbital asphericity. *Nat. Commun.* **2018**, *9*, 1648. [CrossRef] [PubMed]
34. Ma, X.; Yu, G.; Tang, C.; Li, X.; He, C.; Shi, J.; Wang, K.L.; Li, X. Interfacial Dzyaloshinskii-Moriya Interaction: Effect of 5d Band Filling and Correlation with Spin Mixing Conductance. *Phys. Rev. Lett.* **2018**, *120*, 157204. [CrossRef] [PubMed]
35. Kasukawa, S.; Shiota, Y.; Moriyama, T.; Ono, T. Evaluation of electric field effect on interface magnetic properties by propagating spin wave in Pt/Co/MgO structures. *Jpn. J. Appl. Phys.* **2018**, *57*, 080309. [CrossRef]
36. Kim, D.Y.; Kim, N.H.; Park, T.K.; Park, M.H.; Kim, J.S.; Nam, Y.S.; Jung, J.; Cho, J.; Kim, D.H.; Kim, J.S.; et al. Quantitative accordance of Dzyaloshinskii-Moriya interaction between domain-wall and spin-wave dynamics. *Phys. Rev. B* **2019**, *100*, 224419. [CrossRef]
37. Mokhtari, B.E.; Ourdani, D.; Roussigne, Y.; Mos, R.B.; Nasui, M.; Kail, F.; Chahed, L.; Chérif, S.M.; Stashkevich, A.; Gabor, M. Perpendicular magnetic anisotropy and interfacial Dzyaloshinskii–Moriya interaction in as grown and annealed X/Co/Y ultrathin systems. *J. Phys. Condens. Matter.* **2020**, *32*, 495802. [CrossRef]
38. Pai, C.F.; Mann, M.; Tan, A.J.; Geoffrey, S.D. Beach, Determination of spin torque efficiencies in heterostructures with perpendicular magnetic anisotropy. *Phys. Rev. B* **2016**, *93*, 144409. [CrossRef]
39. Lee, J.M.; Jang, C.; Min, B.C.; Lee, S.W.; Lee, K.J.; Chang, J. All-Electrical Measurement of Interfacial Dzyaloshinskii-Moriya Interaction Using Collective Spin-Wave Dynamics. *Nano Lett.* **2016**, *1*, 62–67. [CrossRef]
40. Kim, S.; Jang, P.H.; Kim, D.H.; Ishibashi, M.; Taniguchi, T.; Moriyama, T.; Kim, K.J.; Lee, K.J.; Ono, T. Magnetic droplet nucleation with a homochiral Néel domain wall. *Phys. Rev. B* **2017**, *95*, 220402. [CrossRef]
41. Ma, C.T.; Zhou, W.; Kirby, B.J.; Poon, S.J. Interfacial mixing effect in a promising skyrmionic material: Ferrimagnetic Mn4N. *AIP Adv.* **2022**, *12*, 085023. [CrossRef]
42. Huyen, N.T.V.; Suzuki, M.; Yamauchi, K.; Oguchi, T. Topology analysis for anomalous Hall effect in the noncollinear antiferromagnetic states of Mn_3AN (A= Ni, Cy, Zn, Ga, Ge, Pd, In, Sn, Ir, Pt). *Phys. Rev. B* **2019**, *100*, 094426. [CrossRef]
43. Quessab, Y.; Xu, J.W.; Ma, C.T.; Zhou, W.; Riley, G.A.; Shaw, J.M.; Nembach, H.T.; Poon, S.J.; Kent, A.D. Tuning interfacial Dzyaloshinskii-Moriya interactions in thin amorphous ferrimagnetic alloys. *Sci. Rep.* **2020**, *10*, 7447. [CrossRef] [PubMed]
44. Ma, C.T.; Xie, Y.; Sheng, H.; Ghosh, A.W.; Poon, S.J. Robust Formation of Ultrasmall Room-Temperature Neél Skyrmions in Amorphous Ferrimagnets from Atomistic Simulations. *Sci. Rep.* **2019**, *9*, 9964. [CrossRef]